Comparison of photothermal and piezoacoustic excitation methods for frequency and phase modulation atomic force microscopy in liquid environments

A. Labuda,[1] K. Kobayashi,[2] D. Kiracofe,[3] K. Suzuki,[2] P. H. Grütter,[1] and H. Yamada[2]

[1]*Department of Physics, McGill University, Montreal, Quebec H3A 2T8, Canada*
[2]*Department of Electronic Science and Engineering, Kyoto University, Japan*
[3]*Birck Nanotechnology Center and Department of Mechanical Engineering, Purdue University, West Lafayette, Indiana, USA.*

In attempting to perform frequency modulation atomic force microscopy (FM-AFM) in liquids, a non-flat phase transfer function in the self-excitation system prevents proper tracking of the cantilever natural frequency. This results in frequency-and-phase modulation atomic force microscopy (FPM-AFM) which lies in between phase modulation atomic force microscopy (PM-AFM) and FM-AFM. We derive the theory necessary to recover the conservative force and damping in such a situation, where standard FM-AFM theory no longer applies. Although our recovery procedure applies to all cantilever excitation methods in principle, its practical implementation may be difficult, or even impossible, if the cantilever is driven piezoacoustically. Specifically, we contrast the piezoacoustic excitation method to the photothermal method in the context of force spectroscopy of hydration structures at the mica-water interface. The results clearly demonstrate that photothermal excitation is superior to piezoacoustic excitation, as it allows for accurate quantitative interpretation of the acquired data. *Copyright 2011 Author(s). This article is distributed under a Creative Commons Attribution 3.0 Unported License.* [doi:10.1063/1.3601872]

I. INTRODUCTION

The benefits of frequency modulation atomic force microscopy[1] (FM-AFM) over amplitude modulation atomic force microscopy[2] (AM-AFM) in vacuum are clear: not only is the response time greatly improved, but the conservative and dissipative forces are decoupled because the cantilever is always driven at its natural frequency, which also maintains the signal-to-noise ratio (SNR) at its maximum throughout the experiment. In this ideal situation, the interpretation of the acquired FM-AFM data is straightforward: the conservative interaction between the cantilever tip and the sample is directly related to the shift in the self-excitation frequency, while the interaction damping is directly related to the drive amplitude of an automatic-gain-controller (AGC) which maintains a constant cantilever amplitude.

In liquid environments, the advantages of FM-AFM are not nearly as clear. Recently, it has been shown that the frequency dependence of the self-excitation electronics and viscous damping can affect the frequency shift and the drive amplitude,[3,4] thereby altering the data acquired by FM-AFM. In fact, as we demonstrate in this article, operating a self-excitation loop in liquids usually results in a modulation of both the cantilever phase and the drive frequency simultaneously because the self-excitation does not properly track the shift in cantilever natural frequency. We refer to this mode of AFM operation as frequency-and-phase modulation atomic force microscopy (FPM-AFM), which lies in between phase modulation atomic force microscopy[5,6] (PM-AFM) and FM-AFM. In this article, we further demonstrate how the behaviour of an AFM operated by

self-excitation (or a phase-locked-loop (PLL)) strongly depends on the cantilever excitation method, and that understanding this behaviour is imperative for proper interpretation of the acquired data.

Choosing the optimal excitation method for cantilever actuation is not always straightforward. There are various trade-offs between the different excitation methods, such as cost, ease of use, implementation, and extraction of physically relevant data. The piezoacoustic method is the most widely used because it inexpensive and easy to operate. However, these considerations are moot if the excitation method causes artefacts that prevent the accurate recovery of physically relevant data. In this article, we compare the piezoacoustic and photothermal[7] methods of excitation with respect to data recovery.

The context used for this comparison is the study of force spectroscopy of hydration layers near a mica surface.[8–10] These spectroscopy measurements, presented in the next section, serve as a motivation for this paper as they clearly demonstrate that instrumental artefacts dominate the acquired data and strongly depend on the excitation method. The subsequent section presents the theory necessary for recovering the conservative force and damping, which are not directly observable during an AFM experiment. During the recovery procedure, we demonstrate difficulties that arise for piezoacoustic excitation due to its highly corrugated and time-varying transfer function, while contrasting to the well-behaved photothermal excitation method. Furthermore, we perform a simulation to demonstrate the practical limits to the damping recovery for piezoacoustic excitation. In the last section, we summarize our findings and extend our conclusions to topography imaging.

II. EXPERIMENTAL DATA

A. Hydration spectroscopy experiment

All data presented in this paper were acquired in aqueous 0.25M KCl on mica, using a modified Shimadzu AFM with home-built self-excitation electronics.[11] The liquid cell was sealed to prevent evaporation. Then, the AFM was left in a temperature-regulated enclosure for 50 hours before starting the experiment. The cantilever (PPP-NCH, NanoSensors) had a natural frequency of 128.8kHz and a quality factor of 7.7 which was measured after approaching the sample (within a tip-sample distance < 100nm). The stiffness of 23.7N/m was determined from a thermal spectrum in air calibrated by a force-distance curve on silicon before the experiment.

Three-dimensional (3D) hydration maps were acquired, as shown in Fig. 1. The particular method of acquisition used here differs slightly from previously reported experiments.[10] Each 3D hydration map is composed of 8320 force spectroscopy profiles in the z direction, taken on an xy grid. A threshold frequency shift limits the extent of each approach distance: once the threshold is exceeded upon approaching, the tip is retracted and the process is repeated at the next (x,y) position. This results in a partially filled 3D matrix; red pixels in Fig. 1 represent pixels that contain no data. The heights at which the threshold is reached are used to correct the data for drift in the z-direction: a slope is fit and subtracted along the fast scan direction (x) and a 2nd order polynomial is fit and subtracted along the slow scan direction (y).

The four hydration maps presented in Fig. 1 were acquired within a total span of 45 minutes. The method of excitation was alternated between piezoacoustic and photothermal to ensure reproducibility of the results. All the control and detection electronics remained identical, and the AGC amplitude set point was kept at 0.33nm (peak-to-peak) for both methods. The only necessary adjustment for each hydration map was the offset of the phase shifter (CD-951V4, NF Corporation) in order to set the starting frequency to 128.2kHz, which was a local minimum in the drive amplitude of the piezoacoustic method near the natural frequency of the cantilever.

The data in Fig. 2(a) are the average measured frequency shift and the average drive amplitude for the four hydration maps in Fig. 1. Both methods generated reproducibly different results. Presumably, a slight tip change occurred before the last photothermal dataset (PT02) which reduced the measured distance between hydration layers and improved the imaging quality as seen in Fig. 1. Nevertheless, whereas the frequency shift profiles roughly differ by a scalar between both methods, the drive amplitude shows qualitatively very different results.
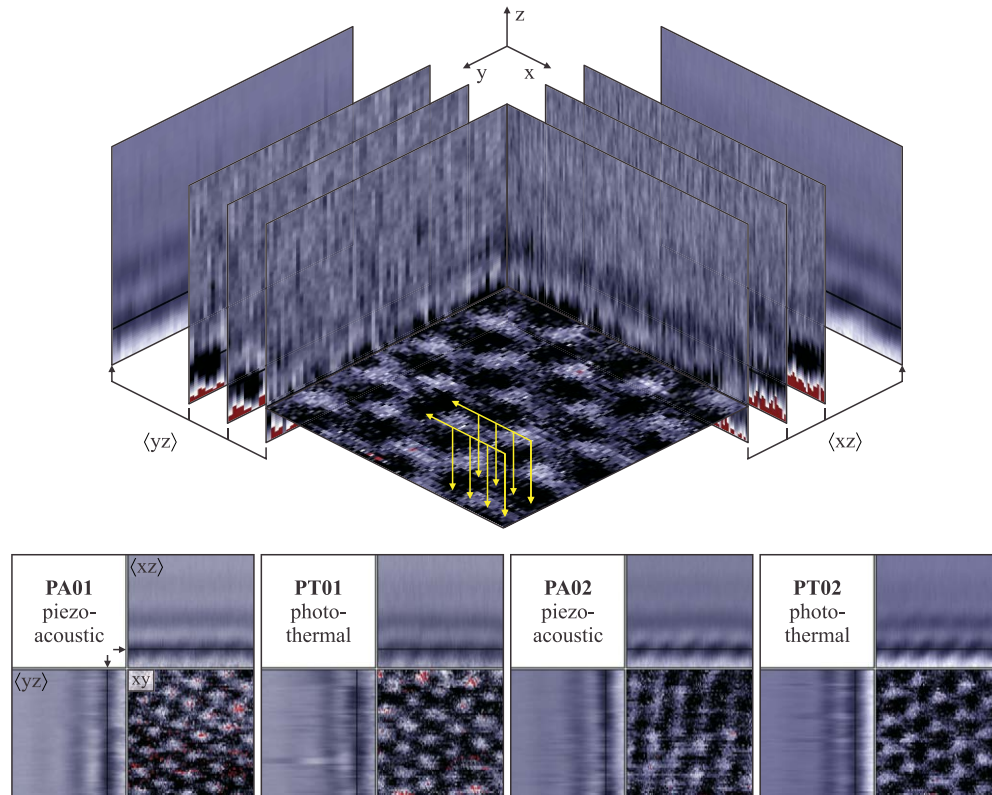
FIG. 1. 3D frequency shift maps were acquired in 0.25M KCl at the mica interface. *Top*: The acquisition process is illustrated by the yellow arrows. Data was acquired by raster scanning, with z as the fastest direction and y as the slowest. Red pixels contain no data: the frequency shift threshold had been reached and the sample was already retracted for that (x,y) position. The xz and yz planes were averaged for display, while a single xy cross-section is shown. *Bottom*: Four 3D frequency shift maps are labelled according to the method of cantilever excitation. All four hydration maps were acquired within 45 minutes, each lasting ~4min. The excitation methods were alternated to test for reproducibility. Dimensions in pixels: $128 \times 65 \times 119$. Nominal dimensions in nm: $2.2 \times 1.7 \times 1.1$. Amplitude set point: 0.33nm peak-to-peak.

Why are there repeatable measurable differences between both excitation methods if the tip-sample interactions are the same?

Before answering this question, it must be noted that both signals of interest to the AFM user, the cantilever natural frequency shift $\Delta\omega_o$ and the damping γ_{tip} due to tip-sample interactions, are *not* directly experimentally observable during an AFM experiment. The measured frequency shift $\Delta\omega$ can differ from the actual cantilever natural frequency $\Delta\omega_o$, and the measured drive amplitude V_d of the AGC can differ from the actual damping γ_{tip}. The relationship between these signals strongly depends on the cantilever excitation method and the self-excitation electronics. Fig. 3 illustrates how these two pairs of signals are separated by the transfer functions of the self-excitation system.

The differences in Fig. 2(a) can therefore be understood by attempting to recover the two signals of physical interest: 1) the cantilever natural frequency shift $\Delta\omega_o$, which is the measure of conservative tip-sample forces, will be obtained after measuring the *phase* transfer function of the self-excitation loop; 2) the damping γ_{tip} will be retrieved by a further analysis of the *amplitude* transfer functions of the excitation and detection systems.

B. AFM characterization

The recovery procedure presented in the next section requires a characterization of the AFM system, which is summarized in this subsection.
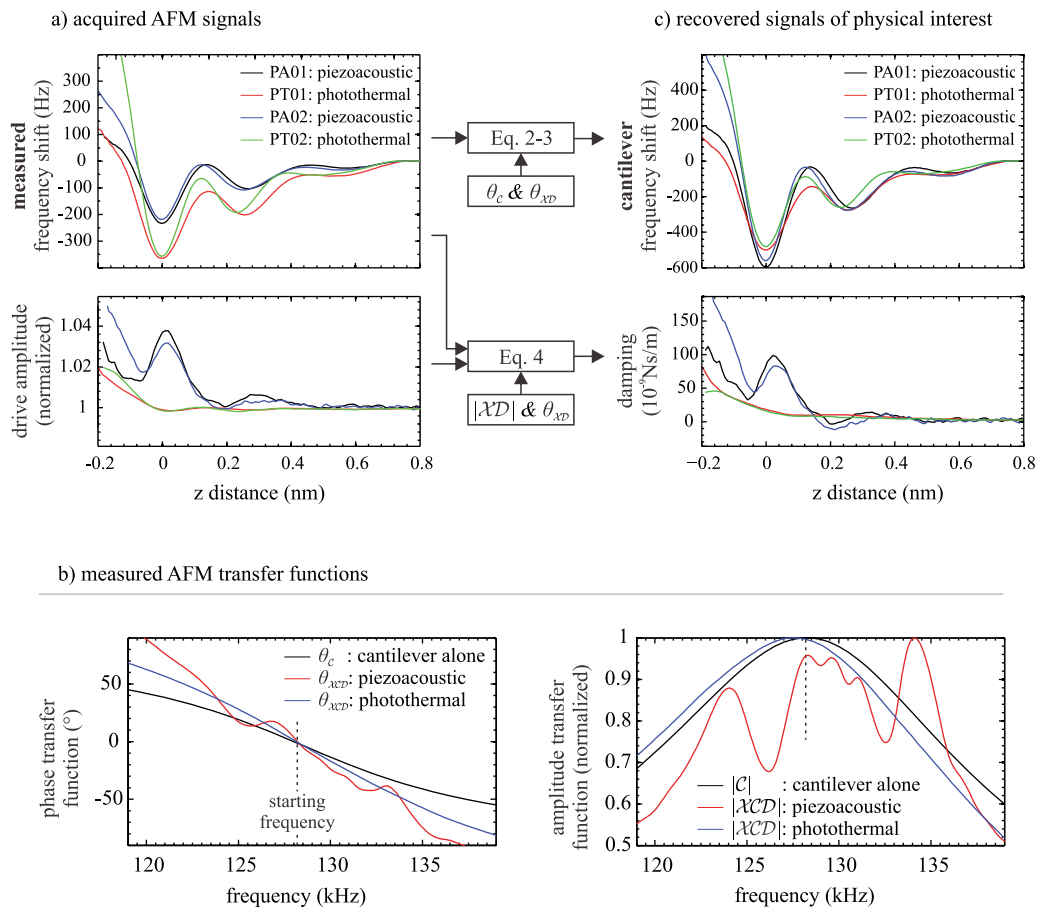
FIG. 2. a) The frequency shift and drive amplitude channels were acquired during the four 3D hydration maps in Fig. 1, and were averaged over all (x,y) positions for display on this plot. The height at the most negative frequency shift of each curve was arbitrarily set to z=0nm. b) Phase (*top*) and amplitude (*bottom*) transfer functions of the cantilever alone, and for a cantilever driven by the piezoacoustic and photothermal excitation systems. All transfer functions were acquired <100nm away from the surface after the acquisition of the data in (a). c) *top*: Recovered cantilever frequency shift $\Delta\omega_o$ from the measured frequency shift $\Delta\omega$ in (a) by using the phase transfer functions in (b). *bottom:* Recovered damping signal from the drive amplitude in (a) by using both transfer functions in (b).

Using a network analyzer (Agilent 4395A), the driven response of the cantilever was measured. This results in the combined transfer function $\mathcal{XCD}$, as can be understood from Fig. 3. The transfer function of the excitation system $\mathcal{X}$ can be isolated by independently measuring the transfer function of the detection and filtering system $\mathcal{D}$, and the transfer function of the cantilever $\mathcal{C}$. The transfer function $\mathcal{D}$ was independently measured with the network analyzer (not shown), while $\mathcal{C}$ was deduced from the thermal power spectrum of the cantilever (see Appendix A 1 for details). Assuming a flat phase transfer function of the phase shifter, which was verified to be a good approximation on our system, completes the characterization of the AFM. The results are presented in Fig. 2(b).

The following notation will be used for transfer functions: $\theta_{\mathcal{XD}}$ and $|\mathcal{XD}|$ represent the phase and amplitude transfer functions of the complex-valued transfer function $\mathcal{XD}$. Furthermore, transfer functions will be combined or isolated from the above-mentioned measurements, as in $|\mathcal{XD}| = |\mathcal{XCD}| / |\mathcal{C}|$ and $\theta_{\mathcal{XD}} = \theta_{\mathcal{XCD}} - \theta_{\mathcal{C}}$, for example.
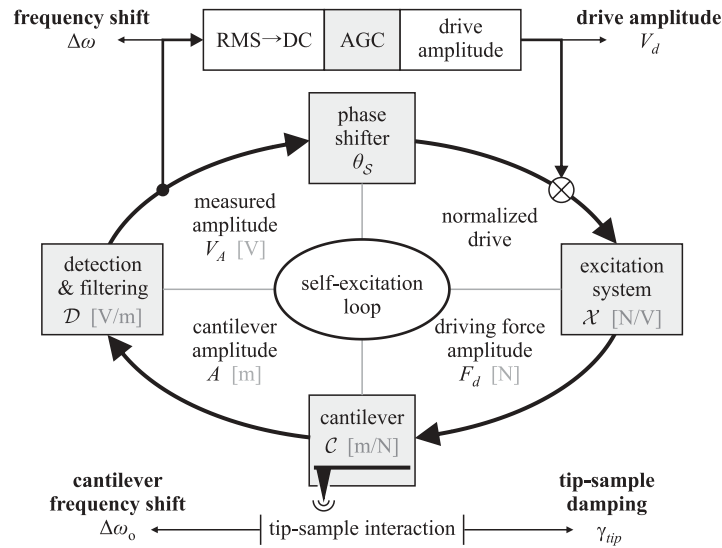
FIG. 3. Diagram of the self-excitation loop used in the derivation of FPM-AFM theory. The evolution of the signal is shown inside the loop, along with units. The total transfer function of the loop is divided into four subunits (grey boxes). The AGC is a side loop which maintains a constant cantilever measured amplitude V_A. The variables of scientific interest are shown on the bottom, while the experimental observables are shown on the top.

III. THEORY AND SIGNAL RECOVERY

In the following two subsections, we derive the theory necessary to recover the signals of physical interest ($\Delta\omega_o$ and γ_{tip}) from the acquired signals ($\Delta\omega$ and V_d) by solving the system of transfer functions presented in Fig. 3. In the process, we demonstrate the recovery procedure on the spectroscopy data presented in the previous section and discuss differences between the piezoacoustic and photothermal methods of excitation. In the last subsection, we discuss the fundamental difficulties that prevent the recovery of damping in the case of piezoacoustic excitation.

A. Recovery of the conservative interaction

The cantilever natural frequency shift $\Delta\omega_o$ differs from the measured self-excitation frequency shift $\Delta\omega$ because the instrumental phase spectrum $\theta_{\mathcal{XD}}$ is not flat. Relating $\Delta\omega_o$ to $\Delta\omega$ begins with an explanation of the self-excitation method.

The key component of the self-excitation loop is the cantilever, whose interaction with a sample affects the resonant behaviour of the entire loop. By positive feedback, the self-excitation loop spontaneously oscillates at the frequency for which the total phase of all four loop elements $\theta_{\mathcal{XCDS}} = -360°$, as can be deduced from Fig. 3. Typically, the phase shifter ($\theta_{\mathcal{S}}$) inside the loop is adjusted to set the starting self-excitation frequency near the cantilever natural frequency, such that $\theta_{\mathcal{C}} = -90°$ before the experiment. Ideally, the self-excitation frequency tracks the cantilever natural frequency, which varies due to tip-sample conservative forces, to maintain $\theta_{\mathcal{C}} = -90°$ throughout the experiment. In reality, because $\theta_{\mathcal{XCDS}} = -360°$ and $\theta_{\mathcal{S}}$ remains constant, any frequency dependent change in the phase $\theta_{\mathcal{XD}}$ of the excitation and detection systems is compensated by a change in the cantilever phase $\theta_{\mathcal{C}}$ during the experiment,[4] *i.e.*

$$\Delta\theta_{\mathcal{C}} = -\Delta\theta_{\mathcal{XD}}. \tag{1}$$

Because this shift in cantilever phase is caused by the measurable phase spectrum $\theta_{\mathcal{XD}}$, it can be predicted before the experiment. During the experiment, $\Delta\omega$ deviates from $\Delta\omega_o$ upon interaction with the sample because the self-excitation system drives the cantilever off-resonance according to
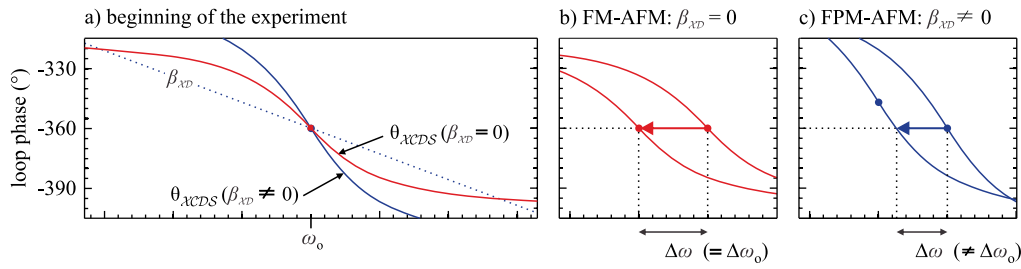
FIG. 4. The phase spectrum of the entire self-excitation loop $\theta_{\mathcal{XCDS}}$ is shown for two cases: 1) *Red*: $\theta_{\mathcal{XD}}$ is flat with a slope $\beta_{\mathcal{XD}} = 0$, and 2) *Blue*: $\beta_{\mathcal{XD}} \neq 0$. In both cases, the phase shifter was adjusted to make the cantilever natural frequency ω_o fulfill the self-excitation condition $\theta_{\mathcal{XCDS}} = -360°$. The dots on the curves represent positions where the cantilever phase $\theta_{\mathcal{C}} = -90°$. b) In the case of FM-AFM, where $\beta_{\mathcal{XD}} = 0$, the self-excitation frequency tracks the variable cantilever natural frequency during conservative tip-sample interactions, so $\Delta\omega = \Delta\omega_o$. c) In the case of FPM-AFM, the non-zero slope $\beta_{\mathcal{XD}} \neq 0$ offsets the perturbed natural frequency (blue dot) away from $\theta_{\mathcal{XCDS}} = -360°$ upon interaction. Then, the self-excitation loop resonates off the cantilever resonance, and $\Delta\omega \neq \Delta\omega_o$.

the phase shift defined by Eq. (1), resulting in the following relationship:

$$\Delta\omega_o = \Delta\omega + \frac{\Delta\theta_{\mathcal{XD}}(\Delta\omega)}{\beta_{\mathcal{C}}}, \tag{2}$$

where $\beta_{\mathcal{C}} = -\frac{2Q}{\omega_o}$ is the slope of the cantilever phase spectrum - approximated as linear and constant in this particular case. Note that $\Delta\theta_{\mathcal{XD}}$ is a function of $\Delta\omega$, not $\Delta\omega_o$.

Fig. 2(b) shows the empirically measured $\theta_{\mathcal{XD}}$ for both the piezoacoustic and photothermal excitation methods. Notice that the piezoacoustic $\theta_{\mathcal{XD}}$ is highly corrugated, therefore Eq. (2) must be solved numerically. On the other hand, the photothermal $\theta_{\mathcal{XD}}$ can be described by a linear slope $\beta_{\mathcal{XD}}$ within the bandwidth of the experiment. Parametrically fitting the acquired phase spectrum reduces the effects of noise, with a negligible loss in accuracy. This results in a special case of Eq. (2), where $\Delta\theta_{\mathcal{XD}} = \beta_{\mathcal{XD}} \times \Delta\omega$, such that

$$\Delta\omega_o = \frac{\beta_{\mathcal{XCD}}}{\beta_{\mathcal{C}}}\Delta\omega, \tag{3}$$

where $\beta_{\mathcal{XCD}} = \beta_{\mathcal{C}} + \beta_{\mathcal{XD}}$ is the slope of the phase response $\theta_{\mathcal{XCD}}$ of the driven cantilever. This correction is illustrated in Fig. 4.

These numerical (Eq. (2)) and parametric (Eq. (3)) corrections were performed on the piezoacoustic and photothermal datasets in Fig. 2(a), respectively, by using the measured phase spectra from Fig. 2(b). The results are shown in Fig. 2(c), where the cantilever frequency shifts of both excitation methods overlap reasonably well.

A single number, the β-factor in Eq. (3), summarizes the photothermal correction. The cantilever frequency shift $\Delta\omega_o$ was 1.35× larger than the measured frequency shift $\Delta\omega$. The non-zero $\beta_{\mathcal{XD}}$ is attributable to the band-pass filter (Q~2), which was necessary to avoid excitation of other cantilever bending modes, as well as to the time delay in the photothermal excitation of the cantilever.[12] On the other hand, the numerical piezoacoustic correction cannot be summarized by a single number; but for comparison, it can be noted that $\Delta\omega_o$ was on average 2.6× larger than $\Delta\omega$. This large correction factor is caused by the steep phase spectrum of the piezoacoustic excitation transfer function, as seen in Fig. 2(b).

Having recovered the cantilever frequency shift $\Delta\omega_o$, the established FM-AFM force deconvolution methods[13,14] can be used to obtain the hydration force profiles normal to the mica interface (not shown). Using $\Delta\omega$ rather than $\Delta\omega_o$, by falsely assuming true FM-AFM, would have resulted in a significant underestimation of the conservative interaction and highly inconsistent data between both methods of excitation.

Note that the piezoacoustic experiment was closer to PM-AFM than to FM-AFM because the piezoacoustic phase spectrum was steeper than the cantilever phase spectrum: only ∼40% of the cantilever frequency shift was tracked by the self-excitation process, resulting in a large modulation of the cantilever phase. Despite the recovery of the cantilever frequency shift profiles, there still remain noticeable differences between both methods, as seen in Fig. 2(c). It is likely that the piezoacoustic phase spectrum changed during the time between the hydration experiment and the measurement of the excitation transfer function. This problem will be thoroughly investigated in the context of damping recovery, where it becomes even more pronounced.

Lastly, we warn the reader about the applicability of the theory presented in this subsection. We have taken advantage of the fact that the damping due to tip-sample interactions was *much* smaller than the intrinsic cantilever damping in our particular experiment, allowing the assumption that $\beta_{\mathcal{C}}$ remains constant throughout the experiment. Lifting this restriction leads to a more mathematically involved derivation presented in the Appendix A 2, which takes into account the coupling of the conservative and dissipative interactions. Note that starting the experiment on-resonance does *not* decouple the conservative and dissipative interactions; however, the derivation in the Appendix handles this problem.

B. Recovery of the dissipative interaction

Recovering damping γ_{tip} from the drive amplitude V_d requires the amplitude response of the cantilever driven by both the photothermal and piezoacoustic excitation systems $|\mathcal{XCD}|$. These transfer functions are shown in Fig. 2(b), where the "forest of peaks" problem[15] clearly afflicts piezoacoustic excitation. Before proceeding, a simple experiment will be presented which demonstrates how this highly corrugated transfer function affects the drive amplitude for piezoacoustic excitation. This will clearly demonstrate the necessity for the damping recovery equation presented afterwards.

Dynamic approach curves were acquired at two starting frequencies labelled in Fig. 5(a), with the results shown in Fig. 5(b). Whereas the frequency shift profiles exhibit similar (in-phase) oscillatory behavior, the drive amplitude oscillations are inverted (out-of-phase) between both experiments. This inversion can be understood by examining the amplitude transfer function $|\mathcal{X}|$ in Fig. 5(a). Due to spurious resonances (i.e. the "forest of peaks"), the piezoacoustic excitation system is more efficient at driving the cantilever at some frequencies than at others. When a negative frequency shift occurs, the excitation efficiency may increase or decrease depending on the shape of $|\mathcal{X}|$. For the data begun at 133.35 kHz, a negative frequency shift coincided with a decrease in excitation efficiency, as seen in Fig. 5(a); therefore, the drive amplitude increased to maintain a constant cantilever oscillation amplitude. The opposite occurred for the acquisition started at 125.65 kHz, which resulted in the inversion labelled in Fig. 5(b). Of course, these changes in drive amplitude have nothing to do with tip-sample damping and must be corrected.

Typically, an AFM user calibrates the drive amplitude at the start of the experiment at a single frequency – the starting self-excitation frequency ω_s. The calibration factor is simply the ratio of the cantilever intrinsic damping γ_s (or dissipated power) to the drive amplitude V_s measured at the start of the experiment: γ_s/V_s, where γ_s is calculated by using the parameters obtained by fitting the thermal power spectrum of the cantilever (see Appendix A 1). However, this calibration factor has a strong frequency dependence and therefore does not apply for frequencies other than ω_s. To date, this frequency dependence has been disregarded in all but one FM-AFM derivation[16] to the knowledge of the authors. As demonstrated in Fig. 5, proper interpretation of the drive amplitude relies on the characterization of this frequency dependence.

In the Appendix, we derive the recovery equation for damping, and simply present and explain the result in this section. To summarize, five frequency dependent factors affect the measured normalized drive amplitude Λ (we define the normalized drive amplitude $\Lambda = V_d/V_s$, where V_s is the drive amplitude at the start of the experiment). After characterizing the transfer functions of self-excitation system, an accurate damping signal due to tip-sample interaction γ_{tip} can be recovered by
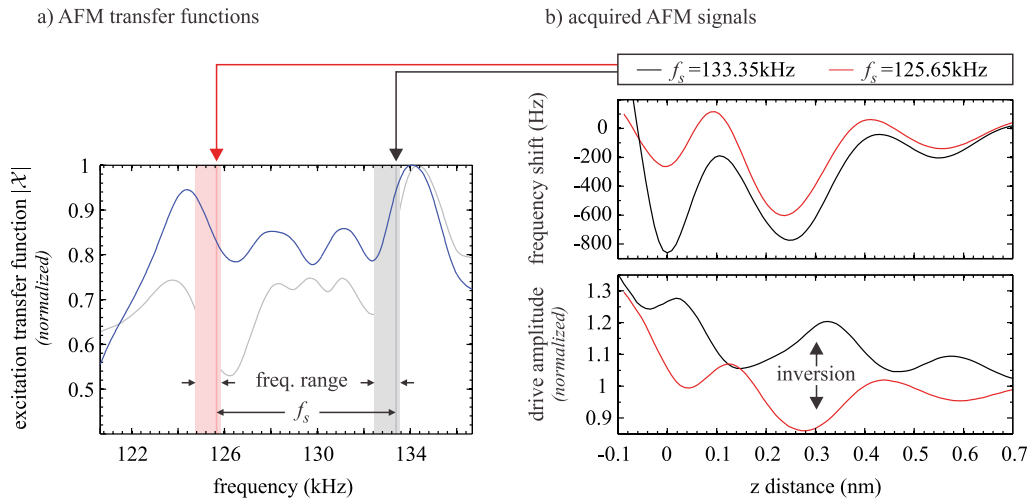
a) AFM transfer functions

b) acquired AFM signals

FIG. 5. a) In *blue*, the amplitude transfer function $|\mathcal{X}|$ of the piezoacoustic excitation system taken just before the data acquired in (b). b) Measured frequency shift and normalized drive amplitude Λ for hydration maps performed at two starting frequencies $f_s (= \omega_s/2\pi)$. Both starting frequencies and frequency ranges are indicated in (a): the *red* dataset was acquired where $|\mathcal{X}|$ had a negative slope, while the *black* dataset was acquired where the $|\mathcal{X}|$ had a positive slope. The opposite slopes for both datasets caused an inversion in the drive amplitude, as labelled. Also noteworthy is that the *blue* transfer function in (a) was taken one day after the transfer functions in Fig. 2(b), of which $|\mathcal{X}|$ is plotted here in *light grey* for comparison. It has changed significantly overnight, even though the entire AFM remained idle inside a temperature regulating enclosure for three days.

$$\gamma_{tip} = \gamma_s \left(\Lambda \frac{\omega_s}{\omega} \left| \frac{\mathcal{X}}{\mathcal{X}_s} \right| \left| \frac{\mathcal{D}}{\mathcal{D}_s} \right| \left| \frac{\sin \left(\theta_{\mathcal{C}s} - \Delta\theta_{\mathcal{X}\mathcal{D}}\left(\omega\right)\right)}{\sin\left(\theta_{\mathcal{C}s}\right)} \right| - \frac{\gamma}{\gamma_s} \right). \tag{4}$$

where every subscript "s" refers to a variable measured at the start of the experiment before tip-sample interaction,

ω is the measured self-excitation frequency,
γ is the frequency dependent intrinsic damping of the cantilever evaluated at ω,
$|\mathcal{X}|$ is the amplitude transfer function of the excitation system evaluated at ω,
$|\mathcal{D}|$ is the amplitude transfer function of the detection system evaluated at ω,
$\theta_{\mathcal{C}s}$ is the cantilever phase at the start of the experiment, and
$\Delta\theta_{\mathcal{X}\mathcal{D}}$ is the change in the phase spectrum of the excitation and detection systems, relative to the phase at the start of the experiment.

The ω_s/ω factor in Eq. (4) is well-known from FM-AFM theory and it corrects for the expected change in drive amplitude due to the velocity dependence of linear viscous damping.[3,17] The other three multiplicative factors - adjacent to ω_s/ω - correct for changes in the drive amplitude Λ which are caused by the frequency dependent calibration of the instrument and will be discussed in the following three paragraphs. After calibrating the drive amplitude Λ, the γ/γ_s factor is subtracted to remove the frequency dependent intrinsic cantilever damping which is not related to tip-sample physics; this factor was numerically computed using Sader hydrodynamic theory.[18] Lastly, γ_s assigns units of damping to the remainder of the calibrated drive amplitude.

The excitation factor, $|\mathcal{X}/\mathcal{X}_s|$, was demonstrated earlier in this section in the case of piezoacoustic excitation. As shown, it arises because the piezoacoustic drive is more or less efficient at different frequencies due to spurious resonances. Although the slope of $|\mathcal{X}/\mathcal{X}_s|$ is one or two orders of magnitude smaller for photothermal excitation, it should not be neglected. It arises because of

the finite diffusion time of thermal gradients within the cantilever,[12] and possibly due to a frequency dependence in the electronics used to modulate the excitation laser.

The detection factor, $|\mathcal{D}/\mathcal{D}_s|$, corrects for a non-ideal response of the detection system. In our AFM, for example, the cantilever deflection signal is band-pass filtered to improve the stability of the self-excitation loop. Once the self-excitation frequency shifts away from the filter's center frequency, the deflection signal is attenuated. In that case, the AGC increases the drive amplitude simply to maintain a constant *measured* cantilever amplitude, resulting in an increased *true* cantilever amplitude. The detection factor accounts for this change in true cantilever amplitude, and corrects the associated change in drive amplitude.

The last factor in Eq. (4), the phase factor, corrects for the self-excitation frequency not tracking the cantilever natural frequency. As it was demonstrated in the previous subsection, even if the cantilever is excited at its natural frequency at the start of the experiment, the self-excitation system cannot track the perturbed natural frequency during the experiment if $\theta_{\mathcal{XD}}$ is not flat. In that case, an increase in drive amplitude is expected simply because driving a cantilever off-resonance is less efficient. This does not constitute a problem if $\theta_{\mathcal{XD}}$ is accurately measured and Eq. (4) is used. Notice that this phase correction factor is the only factor which drops out if true FM-AFM is achieved, therefore Eq. (4) applies to all situations that employ a self-excitation loop (or PLL) and an AGC.

Eq. (4) was used to convert the drive amplitude Λ in Fig. 2(a) into the damping γ_{tip} shown in Fig. 2(c). In contrast to the recovered cantilever frequency shifts, the recovered damping signals for the photothermal and piezoacoustic excitation methods differ significantly. The photothermal damping signal is expected to be very accurate because the associated transfer function can be described parametrically and remains constant with time. Therefore, it appears that the recovery procedure has failed for the piezoacoustic excitation experiment. In the next section, we investigate a possible reason for this failure, and consider whether this failure is a result of our particular experimental setup or a limitation of the piezoacoustic method in general.

Additional note - It remains unclear what proportion of the measured damping occurred due to non-conservative forces. It is possible that conservative forces cause a non-linear response of the cantilever, which can transfer energy to higher harmonics.[19,20] The response of higher harmonics would have to be measured to reach such a conclusion. This justifies our careful wording when introducing the variable γ_{tip}: "damping due to tip-sample interaction". It is *not* solely the damping caused by energy dissipation at the tip-sample junction, and therefore should always be carefully interpreted. However, the fact that the photothermal damping profiles are monotonic, whereas the interaction stiffness is very oscillatory, suggests that the effect of higher harmonics is small, in this particular case.

C. Practical limitations to damping recovery for piezoacoustic excitation

It is worth investigating the degree to which the effects of piezoacoustic excitation on the drive amplitude can be corrected by measuring the transfer function of the excitation system. In this section, we discuss one of many reasons for which the damping recovery for piezoacoustic excitation can fail and result in problematic damping artefacts: the amplitude transfer function of the excitation system $|\mathcal{X}|$ drifts in between its measurement and the time of the experiment. A very slight drift of $|\mathcal{X}|$ in frequency space can distort the damping recovery summarized by Eq. (4). To put this problem into perspective, both excitation spectra in Fig. 5(a) were acquired 20 hours apart, after the entire AFM had already been inside a temperature-regulated enclosure for 50 hours. The large change in amplitude and position of the peaks suggests that even if $|\mathcal{X}|$ is acquired immediately after a given image or approach curve, it *may* not describe the system used during the experiment and prevent an accurate recovery of the damping signal. The exact cause of the observed changes in $|\mathcal{X}|$ is not clear; however, we suspect they are due to thermal drift of the liquid cell. A 40mK drift in the temperature of a 2cm wide liquid cell is expected to cause a 10Hz drift in a fluid-borne resonance around 150kHz simply due to the temperature dependence of the acoustic velocity of water. Such temperature fluctuations are unavoidable throughout the duration of a typical experiment, especially because the laser used for detection and excitation is subject to slow power fluctuations, and the temperature-regulating enclosure has a finite response time to changes in room temperature.
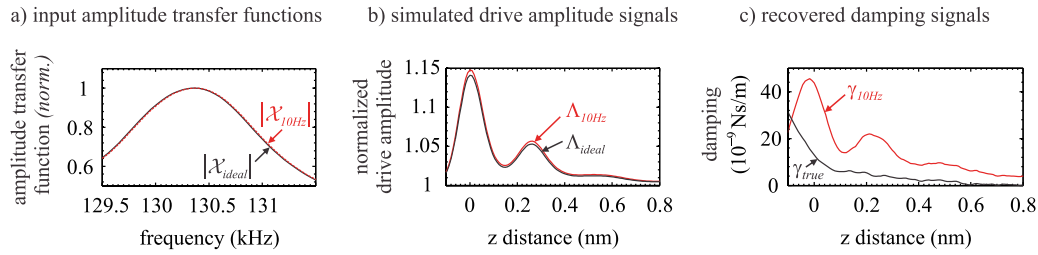
FIG. 6. *In black*, the measured excitation transfer function $|\mathcal{X}_{ideal}|$ in (a) was used to simulate a drive amplitude Λ_{ideal} in (b), and a damping signal γ_{true} was subsequently recovered in (c). In this control experiment, γ_{true} was perfectly recovered because we assumed $|\mathcal{X}_{ideal}|$ was perfectly measured. *In red*, this simulation was repeated by assuming that the AFM user was unaware of a 10Hz drift in the measurement of the amplitude spectrum. Although both spectra in (a) are visually nearly indistinguishable and both resulting drive amplitude signals are only slightly different in (b), the recovered damping signals differ significantly in (c).

Two simulated experiments are now performed to demonstrate the impact of drift on the recovery of the damping signal. As a control, the first simulation assumes no drift in $|\mathcal{X}|$. The second simulation assumes a 10Hz drift which can easily occur even if $|\mathcal{X}|$ is measured immediately after the experiment. For simplicity, we assume the cantilever natural frequency is perfectly tracked by the self-excitation system; in other words, we assume true FM-AFM. To make the simulation experimentally relevant, the cantilever frequency shift and damping from Fig. 2(c) (PT02 dataset) was used as an input and considered the "true" signals. Also, an amplitude transfer function was empirically measured around 130kHz, shown in Fig. 6(a).

The normalized drive amplitude was simulated by solving for Λ in Eq. (4). Fig. 6(b) demonstrates the resulting drive amplitude in the case with no drift (Λ_{ideal}) and in the occurrence of 10Hz drift (Λ_{10Hz}). The two look nearly identical. Next, damping signals were recovered from the simulated drive amplitude signals, using Eq. (4), by assuming the AFM user is unaware of the 10Hz drift. The result is shown in Fig. 6(c), which clearly exposes the instrumental artifacts caused by a non-ideal characterization of the piezoacoustic transfer function. The recovered damping signals are qualitatively very different: the "true" damping is monotonic while the damping recovered after 10Hz drift is oscillatory.

The recovery of damping is highly sensitive to the input amplitude transfer function $|\mathcal{X}|$ because the drive amplitude Λ is dominated by intrinsic cantilever damping γ, which is large compared to the damping due to tip-sample interaction γ_{tip}. Roughly speaking, if the cantilever damping accounts for ~99% of the drive amplitude, a small error of 0.5% in its measurement results in a significant portion (~50%) of the recovered tip-sample damping. This can change a true monotonic damping signal into an apparent oscillatory one, as it has for the piezoacoustic data in this article.

We conclude that a 10Hz drift in the piezoacoustic transfer function during an experiment can destroy the information necessary for recovering an accurate damping signal. This is worrisome because a 10Hz drift can be caused by a thermal drift on the order of 40mK, which is out of the control of the AFM operator and very difficult to detect.

IV. DISCUSSION

We now return to the original question regarding the observable differences between both methods of excitation seen in Fig. 2(a). The theory we derived and demonstrated in the previous section allows for a concrete explanation of frequency-and-phase modulation atomic force microscopy (FPM-AFM), which we alluded to in the introduction. In the latter subsections, we extend our conclusions to topography imaging, and present potential benefits that can be exploited by deliberately tuning the ratio of frequency-to-phase modulation in FPM-AFM.
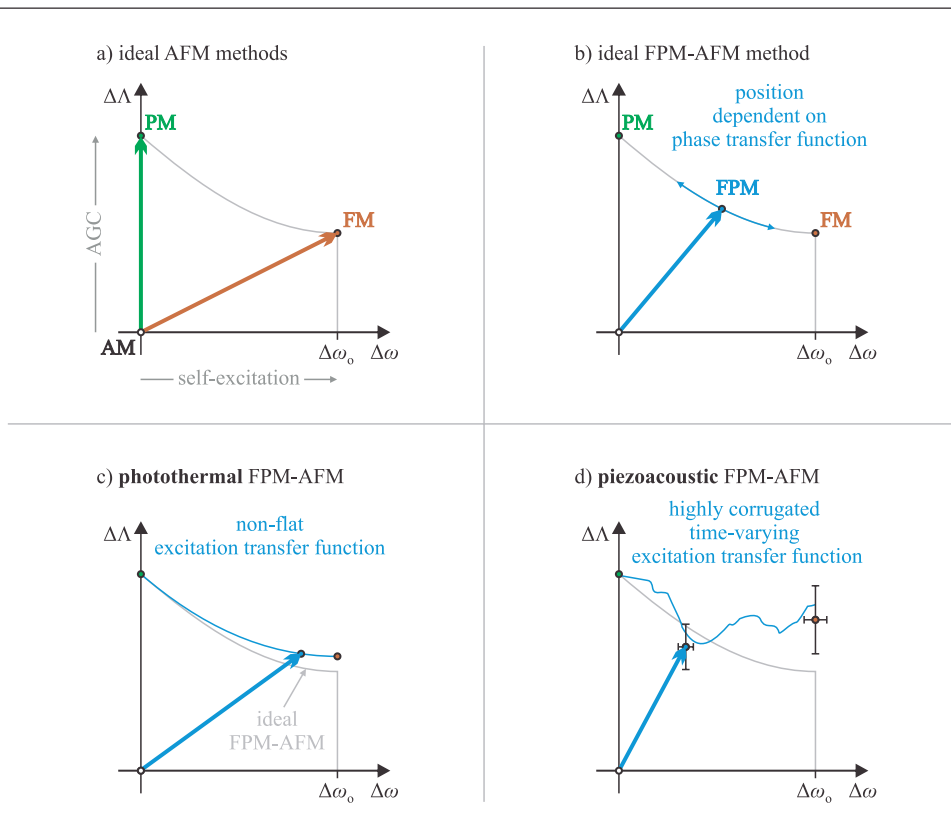
FIG. 7. a) The classical AFM methods of AM, PM, and FM are compared according to the amount of modulation of drive amplitude (y-axis) and drive frequency (x-axis). Note that in FM the drive frequency is modulated to keep cantilever phase constant, which implies $\Delta\omega_o = \Delta\omega$; this also minimizes the drive amplitude modulation because the cantilever is driven on resonance. b) In FPM-AFM, a non-flat phase transfer function in the self-excitation loop causes both the drive frequency and cantilever phase to modulate by some ratio. c) The photothermal data presented in this paper has slight deviation from ideal FPM-AFM, but the position on the graph is easily measurable, allowing the cantilever frequency shift and damping to be recovered. d) The deviation from ideal FPM-AFM is difficult to quantify, because the piezoacoustic transfer function is highly corrugated and time-varying. This leads to an inaccurate recovery of the conservative and dissipative forces. Notice that it is not the shape of the transfer function, but the uncertainty in determining it which causes an inaccurate recovery.

A. Frequency-and-phase modulation (FPM) AFM

The three common modes of AFM operation (AM, FM, PM) are theoretical ideals where only two of the four variables (cantilever amplitude, drive amplitude, cantilever phase, and drive frequency) are modulated during the experiments, while the other two are kept constant. As illustrated in Fig. 7(a), adding an ideal AGC to an AM system converts it to a PM system as it maintains a constant cantilever amplitude by modulating the drive amplitude; further adding an ideal self-excitation loop maintains a constant cantilever phase, and therefore converts an AFM from PM to FM.

However, as we have demonstrated experimentally, this ideal scenario is not necessarily achievable in liquid environments; for example, the electronics may have a non-flat phase spectrum with a slope comparable to that of the cantilever phase spectrum slope. In that case, even if the cantilever phase is set to exactly $-90°$ at the start of the experiment, it will deviate considerably as a function of the frequency shift during the experiment. Consequently, the drive frequency *and* cantilever phase simultaneously modulate during the experiments. As illustrated in Fig. 7(b), such an AFM should be labeled "FPM-AFM" as it actually operates somewhere in between the PM-AFM and FM-AFM methods.

The ratio of phase-to-frequency modulation in the case of FPM-AFM strongly depends on the electronics of the self-excitation loop and the excitation method used to actuate the cantilever. Measuring the appropriate transfer functions of the system allows the acquired data to be properly interpreted using FPM-AFM theory, presented in Section III. Using either PM-AFM or FM-AFM theory can lead to a highly inaccurate interpretation of the tip-sample physics for data acquired on such a system.

Even if they are implemented on the same AFM, the piezoacoustic and photothermal excitation methods operate very differently because their excitation transfer functions differ significantly. The photothermal method can be reliably characterized and lies close to FM-AFM, as shown in Fig. 7(c). On the other hand, the piezoacoustic method was closer to PM-AFM, as shown in Fig. 7(d): the self-excitation loop only tracked ~40% of the cantilever frequency shift, leaving behind ~60% as a cantilever phase modulation for the data in this paper. In either case, measuring the phase spectrum allows the recovery of the cantilever frequency shift which is expected to be very accurate for photothermal excitation, but only somewhat accurate for piezoacoustic excitation. In the latter case, it is not the large deviation from FM-AFM which is problematic, it is only the uncertainty in determining that deviation which prevents an accurate recovery. This uncertainty is depicted as error bars in Fig. 7(d).

In contrast to recovering the cantilever frequency shift in FPM-AFM, the recovery of the damping signal is much more sensitive to the uncertainty in the shape of the excitation transfer function. The root of the problem is that the drive amplitude is dominated by intrinsic cantilever damping that overshadows the damping signal of interest; a small error in characterizing the cantilever damping causes a large error in the recovery of tip-sample damping. This recovery becomes problematic for the piezoacoustic method, where the excitation transfer function is difficult to characterize and may vary in time, preventing the recovery of the damping signal. This problem sets a fundamental limit on the capability of recovering damping for data acquired by piezoacoustic excitation in liquids when the drive frequency is modulated. It should be noted that these problems are above and beyond recovering the cantilever frequency shift. In other words, tracking the cantilever frequency shift perfectly by true FM-AFM is not sufficient for recovering damping accurately.

Finally, we describe both limiting cases of FPM-AFM to relate this entire discussion to the well-established methods of FM-AFM and PM-AFM. The deviation from FM-AFM, as illustrated in Fig. 7(b), can in principle be eliminated by adding a tuneable all-pass filter or a digitally programmable phase shifter inside the self-excitation loop to engineer a flat phase spectrum $\theta_{\mathcal{XD}}$. This recovers the desired condition $\Delta\omega_o = \Delta\omega$ which allows for a direct interpretation of the frequency shift as assumed by FM-AFM. Nevertheless, Eq. (4) must be employed to recover damping because only the phase factor drops out in the case of true FM-AFM. In other words, proper characterization of $|\mathcal{X}|$ and $|\mathcal{D}|$ is necessary for the interpretation of damping in the case of true FM-AFM, for both photothermal and piezoacoustic excitation methods.

The other limiting case, PM-AFM, can be asymptotically reached by setting a very steep instrumental phase spectrum $\theta_{\mathcal{XD}}$ in the self-excitation loop. Then, only the phase factor remains in Eq. (4) while other factors drop out because $\Delta\omega \to 0$. The conservative force can only be recovered after applying Eq. (2) (or by using standard PM-AFM theory if the phase modulation is measured directly during the experiment). In PM-AFM, the loss in signal-to-noise caused by driving the cantilever off resonance is compensated by the fact that drift in $|\mathcal{X}|$ does not prevent the recovery of damping in the context of piezoacoustic excitation.

B. FPM-AFM in topography imaging

So far, we have demonstrated the recovery of the cantilever frequency shift and the damping in the context of force spectroscopy, where the contrast between piezoacoustic and photothermal methods is stark. In topography imaging, the complications discussed in the previous section manifest themselves in more subtle ways because topography imaging is typically performed at a constant frequency shift.

Section III A demonstrated that the self-excitation frequency shift is a poor measure of the conservative interaction with the sample. Two images acquired at the same frequency shift set point

may correspond to very different conservative tip-sample interactions; this can occur if the excitation transfer function drifts in time, the Q factor of the band-pass filter is changed, or the experiment is started at a different self-excitation frequency, for example. Consequently, Eq. (2) is necessary for making meaningful comparisons between images and for quantifying tip-sample forces.

A similar conclusion holds for the interpretation of the drive amplitude acquired alongside a topography image. The strong frequency dependence of the drive amplitude, discussed in Section III B, implies that images acquired at different frequency shift set points should not be quantitatively compared until processed by Eq. (4). For example, increasing the frequency shift set point between images may result in an increase of the drive amplitude on one day, and a decrease on another day, depending only on differences in the shape of $|\mathcal{X}|$.

Lastly, the finite feedback response time in topography imaging may cause transient deviations from the frequency shift set point. As we have demonstrated, the common belief that the frequency shift and drive amplitude channels are decoupled by the self-excitation method may not hold in practice. For example, a positive deviation in frequency shift at a step edge in an image can cause an increase or decrease in the drive amplitude which relates only to the slope of $|\mathcal{X}|$. This may result in contrast inversion between two images that does *not* relate to tip-sample dissipation. Processing the frequency shift "error signal" by Eq. (4) is a necessary step for drawing meaningful conclusions about qualitative observations of the drive amplitude channel.

C. Outlook for FPM-AFM

Although FPM-AFM may seem like an undesirable deviation from FM-AFM, it might be beneficial in certain situations. Whereas PM-AFM offers high stability and remains impervious to transient tip crashes,[5] FM-AFM maximizes the signal-to-noise ratio throughout the experiment.[1] In between both extremes, FPM-AFM provides a knob for controlling the desired ratio of phase to frequency modulation, while retaining an accurate interpretation of the tip-sample physics. Depending on the specific setup, excitation method, and goal of the experiment, optimal performance might be achieved by deliberately tuning the ratio between frequency and phase modulation. This can be accomplished by adjusting a band-pass, low-pass, high-pass or all-pass filter inside the self-excitation loop. For example, some experiments in liquids see large frequency shifts ($>10\text{kHz}$)[21] that may exceed the tracking frequency range of available PLLs. In that case, simply tuning the phase spectrum slope by adjusting a band-pass filter can limit the extent of self-excitation frequency shifts while maximizing the frequency range offered by the PLL. In other situations, problematic mechanical resonances can be avoided by deliberately limiting the frequency range explored by the variable self-excitation frequency.

V. CONCLUSION

In conclusion, a system designed to perform FM-AFM in liquids may actually perform frequency-and-phase modulation atomic force microscopy (FPM-AFM), where the phase and frequency of the cantilever are modulated simultaneously. This prohibits the use of FM-AFM theory in the interpretation of the measurement and requires the use of FPM-AFM theory. The procedure necessary for accurately recovering the conservative force and damping involves analyzing relevant phase and amplitude transfer functions of cantilever and the self-excitation system, and numerically computing the frequency dependence of viscous damping.

The proposed recovery of the cantilever natural frequency shift and damping for photothermal FPM-AFM (including FM-AFM) is expected to be very accurate: the phase and amplitude transfer functions of the excitation and detection systems remain very stable throughout the experiment and are linear across a wide bandwidth, making them easily measurable. On the other hand, for piezoacoustic excitation, a numerical approach is necessary to recover the cantilever frequency shift and damping due to the highly-corrugated transfer function (the "forest of peaks"). This approach can lead to large instrumental artefacts, especially in the damping signal, because the piezoacoustic excitation transfer function varies in time. A simple simulation was performed to demonstrate how a shift in the peak position of as little as 10Hz during the experiment can cause an apparent

oscillatory damping signal. A drift of such magnitude is expected if the average temperature of the liquid cell changes by as little as 40mK, making this problem difficult, if not impossible, to manage.

For these reasons, the authors recommend the use of photothermal excitation for FPM-AFM and FM-AFM in liquids as opposed to piezoacoustic excitation.

APPENDIX

1. Determining the cantilever transfer function from a thermal power spectrum

The cantilever transfer function $\mathcal{C}$, shown in Fig. 2(b), was determined as follows. Brownian motion of the water molecules surrounding the cantilever results in a stochastic driving force which can be determined from the damping by the fluctuation-dissipation theorem.[22] The damping per unit length along the cantilever $\check{\gamma}(\omega)$ can be numerically computed from Sader hydrodynamic theory[18] by

$$\check{\gamma}(\omega) = \frac{\pi}{4}\rho_f b^2 \omega \Gamma_i(\omega | \eta, \rho_f, b)$$

where Γ_i is the imaginary component of the hydrodynamic function, η is the viscosity, ρ_f is the mass density of the fluid, and b is the width of the cantilever. Because the entire length of the cantilever does not oscillate with the same amplitude, it is necessary to weigh the integration of the damping per unit length by the square of the normalized eigenmode shape $|\psi_1(x)|^2$ to obtain the effective damping of the cantilever

$$\gamma(\omega) = \int_0^L |\psi_1(x)|^2 \times \check{\gamma}\,dx = \frac{L}{4} \times \frac{\pi}{4}\rho_f b^2 \omega \Gamma_i(\omega),$$

where the eigenmode shape was normalized[23] such that $\psi_1(L) = 1$. Now, the effective force felt by the tip apex can be described by the thermal force spectrum $F_T(\omega)$, in units of N^2/Hz, whose expectation value is given by the fluctuation-dissipation theorem[24,25] as

$$E(F_T(\omega)) = 4k_B T \gamma(\omega),$$

where k_B is the Boltzmann constant and T is the room temperature. The thermal force spectrum is far from white; it carries a spectral density closer to blue noise because $F_T(\omega) \propto \omega^{\sim 0.53}$ around the resonance frequency in our experiment. Note that neither the motion of the cantilever, nor the driving force is "Brownian" in this case; only the positions of water molecules hitting the cantilever follow Brownian statistics.

When the cantilever is thermally driven, the resulting power spectrum $S_{th}(\omega) = F_T \times |\mathcal{C}|^2$. Averaging many thermal spectra $\langle S_{th} \rangle$ allows to estimate $|\mathcal{C}|$ by

$$|\mathcal{C}| = \sqrt{\frac{\langle S_{th} \rangle}{E(F_T)}}.$$

The complex-valued transfer function $\mathcal{C}$ can be approximated by fitting $|\mathcal{C}|$ to a harmonic oscillator model. It should be noted that the harmonic oscillator model does not accurately describe cantilevers with very low Q values. In that case, the Sader hydrodynamic theory[18] can provide a more accurate description of the cantilever transfer function.

2. Complete derivation of FPM-AFM in viscous media

This section relates the measured normalized drive amplitude Λ to the damping due to tip-sample interaction γ_{tip}. Then, γ_{tip} is used to determine the cantilever natural frequency ω_o^* from the measured self-excitation frequency ω.

Once the AFM user chooses a set point for the measured cantilever amplitude V_A, the AGC maintains that value by continually adjusting the drive amplitude V_d. Both voltages are connected by a series of transfer functions:

$$V_A = |\mathcal{D}|\,|\mathcal{C}|\,|\mathcal{X}|\,V_d, \tag{5}$$

which can be understood by inspection of Fig. 3.

In the limit of an ideal AGC, V_A is constant (note that this does *not* ensure that the cantilever amplitude A is constant). In this case, Eq. (5) can be rewritten as

$$V_d \propto |\mathcal{D}|^{-1}\,|\mathcal{C}|^{-1}\,|\mathcal{X}|^{-1}. \tag{6}$$

Upon tip-sample interaction, the cantilever transfer function is perturbed $\mathcal{C} \to \mathcal{C}^*$, by a change in the natural frequency $\omega_o \to \omega_o^*$ and the damping $\gamma \to \gamma^*$. Measuring the drive amplitude at the start of the experiment V_s, along with both parameters describing the cantilever transfer function $|\mathcal{C}(\omega|\omega_o, \gamma)|$ at the starting self-excitation frequency ω_s, allows to normalize the drive amplitude in Eq. (6), as in

$$\Lambda(\omega) = \frac{V_d}{V_s} = \left|\frac{\mathcal{D}(\omega)}{\mathcal{D}(\omega_s)}\right|^{-1} \left|\frac{\mathcal{C}^*(\omega|\omega_o^*, \gamma^*)}{\mathcal{C}(\omega_s|\omega_o, \gamma_s)}\right|^{-1} \left|\frac{\mathcal{X}(\omega)}{\mathcal{X}(\omega_s)}\right|^{-1}. \tag{7}$$

Note that the subscript "s" in this document refers to quantities measured at the start of the experiment, before any tip-sample interaction.

Because the perturbed cantilever natural frequency ω_o^* is unknown to the AFM user throughout the experiment, it is necessary to rewrite both $|\mathcal{C}|$'s in Eq. (7) as a function of the phase of the cantilever, rather than its natural frequency. This will allow to account for the effects of instrumental phase shifts on the measured drive amplitude V_d, without knowledge of ω_o^*. The magnitude response of a damped harmonic oscillator can be mathematically rewritten from its usual form into

$$|\mathcal{C}(\omega|\theta_{\mathcal{C}}, \gamma)| = -\frac{\sin\theta_{\mathcal{C}}(\omega)}{\omega \cdot \gamma}, \tag{8}$$

where $\theta_{\mathcal{C}}(\omega)$ is the phase spectrum defined by

$$\theta_{\mathcal{C}}(\omega) = \tan^{-1}\left\{-\frac{\omega \cdot \gamma}{k\left[(1 - (\omega/\omega_o)^2)\right]}\right\}, \tag{9}$$

where k is the cantilever stiffness.

This allows to rewrite $|\mathcal{C}|$, in Eq. (7), as a function of the cantilever phase at the start of the experiment ($\theta_{\mathcal{C}s}$), as in

$$|\mathcal{C}(\omega_s|\theta_{\mathcal{C}s}, \gamma_s)| = -\frac{\sin\theta_{\mathcal{C}s}}{\omega_s \cdot \gamma_s}, \tag{10}$$

where the starting cantilever damping is experimentally determined by: $\gamma_s = k/Q/\omega_s$, where Q is the quality factor.

Furthermore, the perturbed $|\mathcal{C}^*|$, in Eq. (7), can be rewritten as a function of the phase spectrum $\theta_{\mathcal{XD}}(\omega)$ of the excitation and detection systems by the aid of Eq. (1): $\Delta\theta_{\mathcal{C}} = -\Delta\theta_{\mathcal{XD}}$. After carefully determining the cantilever phase at the start of the experiment $\theta_{\mathcal{C}s}$, the cantilever phase throughout the experiment $\theta_{\mathcal{C}}(\omega)$ is known as it varies *only* according to $\theta_{\mathcal{XD}}(\omega)$, by

$$\theta_{\mathcal{C}}(\omega) = \theta_{\mathcal{C}s} - \Delta\theta_{\mathcal{XD}}(\omega). \tag{11}$$

By Eq. (8) and (11), the perturbed cantilever transfer function becomes

$$\left|\mathcal{C}^*(\omega|\theta_{\mathcal{C}}, \gamma^*)\right| = -\frac{\sin(\theta_{\mathcal{C}s} - \Delta\theta_{\mathcal{XD}}(\omega))}{\omega \cdot \gamma^*}. \tag{12}$$

Notice that any dependence on ω_o^* is gone once θ_{Cs} and $\theta_{\mathcal{XD}}$ are experimentally measured *before* the experiment. Inserting both Eq. (10) and (12) into Eq. (7), results in

$$\Lambda(\omega) = \frac{\omega}{\omega_s} \frac{\gamma^*}{\gamma_s} \left|\frac{\mathcal{D}}{\mathcal{D}_s}\right|^{-1} \left|\frac{\mathcal{X}}{\mathcal{X}_s}\right|^{-1} \left|\frac{\sin(\theta_{Cs} - \Delta\theta_{\mathcal{XD}})}{\sin(\theta_{Cs})}\right|^{-1}, \tag{13}$$

where the notation has been simplified.

The perturbed cantilever damping γ^* is a sum of the intrinsic cantilever damping γ and added damping due to tip-sample interactions γ_{tip}:

$$\gamma^*(\omega) = \gamma(\omega) + \gamma_{tip}. \tag{14}$$

Notice that the intrinsic damping of the cantilever $\gamma(\omega)$ depends on the self-excitation frequency. The approximation made here is that the damping changes quasi-statically, such that the cantilever remains a damped harmonic oscillator, with a linear transfer function, at any point in time. Furthermore, although we are using the framework of viscous damping to model tip-sample damping γ_{tip}, we are not claiming that the physics of the dissipative process are viscous in nature. Careful interpretation of γ_{tip} is always necessary as our model assumes a velocity-dependent damping mechanism.

Isolating γ_{tip} in Eq. (13) using Eq. (14) results in

$$\gamma_{tip} = \gamma_s \left(\Lambda \frac{\omega_s}{\omega} \left|\frac{\mathcal{D}}{\mathcal{D}_s}\right| \left|\frac{\mathcal{X}}{\mathcal{X}_s}\right| \left|\frac{\sin(\theta_{Cs} - \Delta\theta_{\mathcal{XD}})}{\sin(\theta_{Cs})}\right| - \frac{\gamma}{\gamma_s} \right). \tag{15}$$

For ease of reference, all the approximations that were used to derive Eq. (15) are explicitly enumerated:

1. The cantilever is accurately described as a damped harmonic oscillator for the range of all phases explored during the experiment: $\theta_{Cs} - \Delta\theta_{\mathcal{XD}}(\omega)$. Its linear perturbed transfer function $\mathcal{C}^*$ is fully characterized by two quasi-statically time-varying parameters ω_o^* and γ^*.
2. The remaining transfer functions of the self-excitation loop are linear and stationary throughout the experiment.
3. The phase spectrum of the phase shifter (or PLL) is flat. This assumption can be lifted simply by measuring the phase shifter transfer function and adding it to $\theta_{\mathcal{XD}}(\omega)$.
4. If a PLL is used, it can be modelled as an ideal phase shifter.
5. The AGC is ideal, and maintains a constant *measured* cantilever oscillation amplitude V_A.

Having recovered the perturbed damping γ^* during the experiment, it is now possible to accurately determine the cantilever natural frequency ω_o^*. Equating Eq. (9) and (11), and solving, results in

$$\omega_o^* = \sqrt{\omega^2 - \frac{\omega \cdot \gamma^*}{m_{eff}(\omega) \times tan\{\theta_{Cs} - \Delta\theta_{\mathcal{XD}}(\omega)\}}}, \tag{16}$$

where the frequency dependent effective mass of the cantilever $m_{eff}(\omega)$ can be calculated using Sader hydrodynamic theory[18] or estimated as a constant by $m_{eff} = k/\omega_o^2$. The latter case is often a good approximation because m_{eff} carries a weak frequency dependence (as opposed to γ) for typical cantilevers in most liquids.

Note that the much simpler version of the recovery of ω_o^* presented in section III A was made under the assumption that $\gamma_{tip} \ll \gamma$, which is *very* accurate in our experiment. Many experiments in liquids violate this assumption, in which case Eq. (16) should be used instead.

[1] T. R. Albrecht, P. Grutter, D. Horne, and D. Rugar, J. Appl. Phys. **69**, 668 (1991).
[2] G. Binnig, C. F. Quate, and Ch. Gerber, Phys. Rev. Lett. **56**, 930 (1986).
[3] J. E. Sader and S. P. Jarvis, Phys. Rev. B **74**, 195424 (2006).
[4] K. Kobayashi, H. Yamada, and K. Matsuhige, Rev. Sci. Instrum. **82**, 033702 (2011)
[5] Y. Sugawara, N. Kobayashi, M. Kawakami, Y. J. Li, Y. Naitoh, and M. Kageshima, Appl. Phys. Lett. **90**, 194104 (2007).
[6] T. Fukuma, J. I. Kilpatrick, S. Jarvis, Rev. Sci. Instrum. **77**, 123703 (2006)
[7] G. C. Ratcliff, D. A. Erie, and R. Superfine, Appl. Phys. Lett. **72**, 1911 (1998).
[8] K. Kimura, S. Ido, N. Oyabu, K. Kobayashi, Y. Hirata, T. Imai, and H. Yamada, J. Chem. Phys. **132**, 19470 (2010).
[9] T. Fukuma, K. Kobayashi, K. Matsushige, and H. Yamada, Appl. Phys. Lett. **87**, 034101 (2005).

[10] T. Fukuma, Y. Ueda, S. Yoshioka, and H. Asakawa, Phys. Rev. Lett. **104**, 016101 (2010).

[11] K. Kobayashi, H. Yamada, H. Itoh, T. Horiuchi, and K. Matsushige, Rev. Sci. Instr. **72**, 4383 (2001).

[12] V. Pini, B. Tiribilli, C. M. C. Gambi, and M. Vassalli, Phys. Rev. B **81**, 054302 (2010).

[13] F. J. Giessibl, Appl. Phys. Lett. **78**, 123 (2001).

[14] J. E. Sader and S. P. Jarvis, Appl. Phys. Lett. **84**, 1801 (2004).

[15] T. E. Schaffer, J. P. Cleveland, F. Ohnesorge, D. A. Walters, and P. K. Hansma, J. Appl. Phys. **80**, 3622 (1996).

[16] R. Roger and S. V. Kalinin, Nanotechnology **21**, 455705 (2010).

[17] J. P Cleveland, B. Anczykowski, A. E. Schmid, V. B. Elings, Appl. Phys. Lett. **72**, 2613 (1998).

[18] J. E. Sader, J. Appl. Phys. **84**, 64 (1998).

[19] J. Melcher, C. Carrasco, X. Xu, J. L. Carrascosa, J. Gómez-Herrero, P. J. de Pablo, and A. Raman, Proc. Natl. Acad. Sci. U.S.A **106**, 13655 (2009).

[20] D. Martínez-Martín, C. Carrasco, R. Pérez, M. Mateu, J. Carrascosa, P. de Pablo, J. Gómez-Herrero, D. Kiracofe, J. Melcher, and A. Raman, under review (2011).

[21] W. Hofbauer, R. J. Ho, Hairulnizam R, N. N. Gosvami, and S. J. O'Shea, Phys. Rev. B **80**, 134104 (2009).

[22] M. T. Clark, J. E. Sader, J. P. Cleveland, and M. R. Paul, Phys. Rev. E **81**, 046306 (2010).

[23] J. Melcher, S. Hu, and A. Raman, Appl. Phys. Lett. **91**, 053101 (2007).

[24] M. R. Paul and M. C. Cross, Phys. Rev. Lett. **92**, 235501 (2004).

[25] M. T. Clark, J. E. Sader, J. P. Cleveland, and M. R. Paul, Phys. Rev. E **81**, 046306 (2010).